PCCP

PAPER

View Article Online
View Journal | View Issue

Cite this: *Phys. Chem. Chem. Phys.*, 2024, **26**, 21163

Interplay between anion–receptor and anion–solvent interactions in halide receptor complexes characterized with ultrafast infrared spectroscopies†

Jessika L. S. Dean, Caroline G. Cramer and Joseph A. Fournier *

The competition between host–guest binding and solvent interactions is a crucial factor in determining the binding affinities and selectivity of molecular receptor species. The interplay between these competing interactions, however, have been difficult to disentangle. In particular, the development of molecular-level descriptions of solute–solvent interactions remains a grand experimental challenge. Herein, we investigate the prototypical halide receptor *meso*-octamethylcalix[4]pyrrole (OMCP) complexed with either chloride or bromide anions in both dichloromethane (DCM) and chloroform (trichloromethane, TCM) solvent using ultrafast infrared transient absorption and 2D IR spectroscopies. OMCP·Br^- complexes in both solvents display slower vibrational relaxation dynamics of the OMCP pyrrole NH stretches, consistent with weaker H-bonding interactions with OMCP compared to chloride and less efficient intermolecular relaxation to the solvent. Further, OMCP·Br^- complexes show nearly static spectral diffusion dynamics compared to OMCP·Cl^-, indicating larger structural fluctuations occur within chloride complexes. Importantly, distinct differences in the vibrational spectra and dynamics are observed between DCM and TCM solutions. The data are consistent with stronger and more perturbative solvent effects in TCM compared to DCM, despite DCM's larger dielectric constant and smaller reported OMCP·X^- binding affinities. These differences are attributed to the presence of weak H-bond interactions between halides and TCM, in addition to competing interactions from the bulky tetrabutylammonium countercation. The data provide important experimental benchmarks for quantifying the role of solvent and countercation interactions in anion host–guest complexes.

Received 4th June 2024,
Accepted 23rd July 2024

DOI: 10.1039/d4cp02280g

rsc.li/pccp

I. Introduction

Anion recognition and receptors play critical roles in biological signaling pathways,[1–3] industrial sensing applications,[4–6] and in synthetic strategies for environmental remediation.[7–12] Anion–receptor interactions are typically described in terms of electrostatic interactions, such as H-bonding and halogen bonding, although the importance of nonelectrostatic effects have recently been raised.[13–16] There is continued interest in the supramolecular chemistry community for the development of novel receptor complexes with improved anion selectivity, transport, and sensing properties.[17–22] Many of these complexes are based on the calix[4]pyrrole macrocycle due to their ease of synthesis and chemical modification, leading to, in principle, high tunability of anion binding affinities and selectivity.[23–29] Despite many investigations of calix[4]pyrroles and other macrocyclic anion receptor systems, which have revealed detailed structural information through X-ray crystal structures and binding affinities through solution-phase NMR and isothermal titration calorimetry (see ref. 30, the ESI in ref. 31 and ref. 32–33), important questions still remain regarding the fundamental role of solvent interactions in anion recognition. Specifically, the competition between anion–receptor and anion–solvent interactions is a key component that dictates binding affinities and selectivity.[34–39] The difficulty in probing first solvation shell interactions in bulk solution has made the study of solute–solvent interactions challenging experimentally, preventing more quantitative insights into anion recognition that can lead to the rational design of improved receptor systems.

Several recent studies have been conducted on the simplest calix[4]pyrrole macrocycle, *meso*-octamethylcalix[4]pyrrole (OMCP, Fig. 1a), complexed with various anions isolated in the gas phase to characterize the anion–receptor interactions in the absence of solvent.[40,41] In one study, Terry *et al.* recorded vibrational spectra of cryogenically cooled OMCP·X^- (X = F, Cl, Br) in the pyrrole NH

Department of Chemistry, Washington University in St. Louis, St. Louis, MO 63130, USA. E-mail: jfournier@wustl.edu

† Electronic supplementary information (ESI) available. See DOI: https://doi.org/10.1039/d4cp02280g

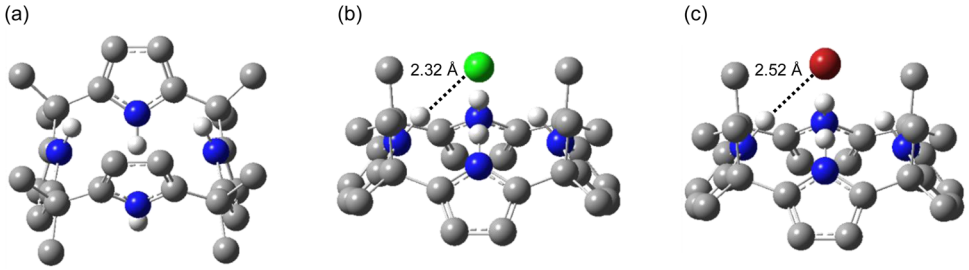

Fig. 1 Minimum-energy structures of (a) OMCP, (b) OMCP·Cl^-, and (c) OMCP·Br^-. Calculated NH···X^- H-bond distances are shown in (b) and (c). H atoms bound to carbon are omitted for clarity.

stretch region.[40] The NH symmetric and antisymmetric stretches in OMCP·Cl^- were measured to be approximately 20 cm^{-1} red shifted compared to those in OMCP·Br^-, consistent with chloride's larger binding affinity with OMCP and smaller NH···Cl^- H-bond distance. The vibrational patterns for both complexes and spectral shifts were well captured by harmonic frequency calculations. OMCP·F^-, on the other hand, did not display obvious NH stretching modes but rather a congested series of transitions in the CH stretch region. High-level anharmonic modeling revealed the presence of significant coupling of the highly red shifted pyrrole NH stretches with overtones and combination bands involving NH bending, CH bending, and low-frequency modes of the macrocycle due to the particularly strong H-bonding interaction between OMCP and F^-. In another study, Cao and Wang reported anion photoelectron spectra of cryogenically cooled OMCP·X^- (X = F, Cl, Br, I, SCN) complexes.[41] In contrast to the expectation of photoelectron spectra similar to those of the solvated anions, the spectra were consistent with a charge-separated OMCP$^+$·X^- species arising from a harpoon-like mechanism. These two recent studies highlight the strong interactions between OMCP and various anions in the absence of competing solvent interactions.

Although directly studying solute–solvent interactions and disentangling first solvation shell interactions from the bulk solvent background remains quite challenging experimentally, advanced condensed-phase techniques like ultrafast two-dimensional infrared (2D IR) spectroscopy offer much promise for more detailed investigations into solute–solvent effects. 2D IR enables the acquisition of structural and dynamical information that are not easily obtained from linear IR spectra, such as frequency–frequency correlation dynamics and the presence of intra- and/or intermolecular coupling and energy transfer dynamics through the appearance of off-diagonal cross peak features.[42] While rapid advancements in ultrafast IR spectroscopies have enabled detailed investigations of ion–water interactions in bulk aqueous solutions,[43–45] hydration effects in confined environments,[44,46,47] and anisotropic solvation environments around biomolecules,[48,49] characterizing solvent interactions around complex molecular species remains far from general.

Herein, we report ultrafast transient and 2D IR spectra of OMCP·Cl^- and OMCP·Br^- complexes in the pyrrole NH stretch region in two different solvents: dichloromethane (DCM, dielectric constant 8.9) and trichloromethane (TCM, chloroform, dielectric constant 4.7). Vibrational lifetimes, frequency correlation dynamics, and computational predictions employing explicit solvent molecules are used to unravel how the two solvents influence OMCP-halide binding interactions. The data are further used to characterize intermolecular vibrational energy relaxation dynamics and coupling between the OMCP·X^- complexes and the solvent. Importantly, the data show that solvent dielectric constants and anion binding affinities are insufficient in describing halide binding with OMCP and competing solvent interactions in low-dielectric solvents.

II. Methods

The ultrafast infrared spectrometer has been described in detail elsewhere.[50] Briefly, the output of a regenerative amplifier (Coherent Astrella, 800 nm, 30 fs, 1 kHz, 3.6 mJ per pulse) pumped a commercial optical parametric amplifier (light conversion, TOPAS Prime) to generate tunable near-IR signal (1.3–1.45 μm) and idler (1.8–2.1 μm) pulses. The signal and idler pulses were combined in a 1 mm thick $AgGaS_2$ crystal (EKSMA Optics) in a home-built difference frequency generation setup resulting in IR pulses tuned to ~3300 cm^{-1}. The pulse bandwidth was ~300 cm^{-1} with pulse width of about 90 fs.

The IR pulse was first sent through a 1 mm wedged CaF_2 window to generate a probe pulse from the reflection off the front face of the window and a reference pulse from the reflection off the wedged back face. A pump pulse pair was generated and controlled by a mid-IR AOM Ge pulse shaper (PhaseTech). The pump and probe pulses were directed and focused into the sample in the pump–probe geometry. The probe and reference lines were dispersed by a monochromator onto a 128 × 128 pixel MCT focal-plane array detector (PhaseTech), generating the ω_3 detection (probe) axis. For each ω_3 probe frequency at a given pump–probe delay time τ_2, transient absorption signal was recorded for pump pulse i as $-\log[(S_i/R_i)/(R_{i+1}/S_{i+1})]$ where S is the signal monitored by the probe and R the reference pulse.

Transient absorption spectra were collected with the following τ_2 step sizes: −500 to −250 fs in steps of 50 fs, −200 to 500 fs in steps of 20 fs, 550 fs to 1 ps in steps of 50 fs, and 1.2 to 8 ps in steps of 200 fs. 2D IR spectra were generated by monitoring the transient absorption signal at each ω_3 pixel as

a function of the pump pair delay time τ_1, the Fourier transform of which yielded the ω_1 excitation (pump) axis. A τ_1 step size of 4 fs with a rotating frame of 1600 cm^{-1} was used. The τ_1 free-induction decay at each ω_3 pixel was first apodized with a Hanning window and zero-padded to twice the number of points collected for a line spacing of about 6 cm^{-1} along ω_1. The data were interpolated to a 1 cm^{-1} spacing over ω_1 and ω_3. All 2D IR spectra are normalized to 1 with red features corresponding to ground-state bleach signals and blue features corresponding to excited-state absorption signals. The polarization of the probe pulse was controlled using a CdSe zero-order half-wave plate (Alphalas; PO-TWP-L2-25-FIR) and ZnSe polarizer (Edmund Optics; model 62-772). All transient absorption and 2D IR spectra were collected at magic angle (isotropic) polarization.

In the absence of coupling, a 2D IR spectrum consists of negative features along the diagonal (excitation frequency ω_1 = detection frequency ω_3) corresponding to bleaching of the fundamental transitions (ω_{10}) measured in the linear spectrum caused by excitation of ground-state population from the pump pulse. Each bleach transition is accompanied by a positive feature due to the probe pulse causing excitation from $v = 1$ to $v = 2$ following the pump pulse. These excited-state absorption features, therefore, appear at the excited-state frequency (ω_{21}) which, owing to typical anharmonicity in vibrational potentials, fall to lower energies compared to the fundamental bleaches. Features appearing off the diagonal, called cross peaks, indicate the presence of coupling between vibrational modes and/or energy transfer dynamics between modes.[42]

OMCP was purchased from Frontier Specialty Chemicals and used without further purification. The OMCP·Cl^- and OMCP·Br^- complexes were formed by making a 0.1 M OMCP and 0.5 M tetrabutylammonium chloride solution and a 0.1 M OMCP and 0.5 M tetrabutylammonium bromide solution in DCM and TCM. Samples were sandwiched between two 1 mm CaF_2 windows using a 300 μm Teflon spacer in a home-built sample cell. Linear IR spectra of the studied samples were collected on a FTIR spectrometer (Thermo Fisher, Nicolet Summit X) in absorption mode. The measurements done on the heated samples were prepared by resting a plastic-enclosed filled sample cell in an oil bath heated to the reported experimental temperature.

Quantum chemical calculations were performed with Gaussian09[51] at the B3LYP/6-311++G(d,p) level of theory and basis set.

III. Results and discussion

Linear and 2D IR spectra

Calculated minimum-energy structures of bare OMCP, OMCP·Cl^-, and OMCP·Br^- are presented in Fig. 1 and are consistent with X-ray crystal structures[25] and previously reported computational results.[40,52,53] OMCP adopts a 1,3 alternate conformation with an antiparallel arrangement of the pyrrole NH groups (Fig. 1a). H-bonding interactions with anions favor a cone structure with all four NH pyrrole groups binding to the anion (Fig. 1b and c), overcoming the OMCP structural deformation barrier.[52] Chloride forms much stronger H-bond interactions with OMCP compared to bromide, with calculated NH···X^- distances of 2.32 Å and 2.52 Å, respectively. From the gas-phase calculations, the binding energy of chloride with OMCP is 165 kJ mol^{-1} while that for bromide is 133 kJ mol^{-1}. In DCM solvent, chloride has a ~30-fold larger binding affinity with OMCP compared to bromide, corresponding to a free energy difference of −8.8 kJ mol^{-1} between OMCP·Cl^- and OMCP·Br^-.[25]

Calculations were also performed with two explicit TCM and DCM solvent molecules, which are presented in Fig. 2. The presence of the solvent molecules noticeably weakens the OMCP·X^- H-bond, increasing the NH···X^- distances to 2.40 Å and 2.39 Å for chloride in TCM and DCM, respectively, and to 2.62 Å and 2.58 Å for bromide in TCM and DCM, respectively. Additionally, the CH···X^- solvent–halide distances are much shorter (by ~0.1 Å) in TCM compared to DCM and form a nearly linear interaction in TCM, suggestive of a H-bond-like interaction between the halides and the weakly acidic CH group in TCM. These calculations predict, therefore, that TCM interacts more strongly with both halide ions compared to DCM.

FTIR spectra of OMCP·Cl^- and OMCP·Br^- in TCM are presented in Fig. 3a and b, respectively, while those in DCM are given in Fig. 3c and d, respectively. Spectra of OMCP in the absence of the halide salts and the solvent backgrounds are also displayed in each panel of Fig. 3. For the 1,3-alternate configuration of OMCP, a single dominate NH stretch transition is predicted for the isolated molecule (Fig. S1, ESI†) and is consistent with the lone feature observed in solution around

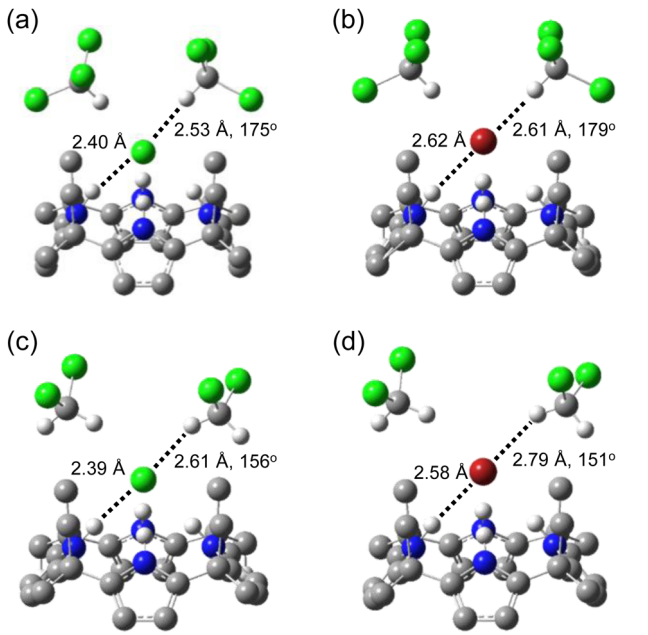

Fig. 2 Minimum-energy structures of OMCP·X^- with explicit solvent molecules. (a) OMCP·Cl^- with TCM. (b) OMCP·Br^- with TCM. (c) OMCP·Cl^- with DCM. (d) OMCP·Br^- with DCM. Calculated NH···X^- distances, CH···X^- distances, and CHX^- angles are shown in each panel. H atoms bound to carbon in OMCP are omitted for clarity.

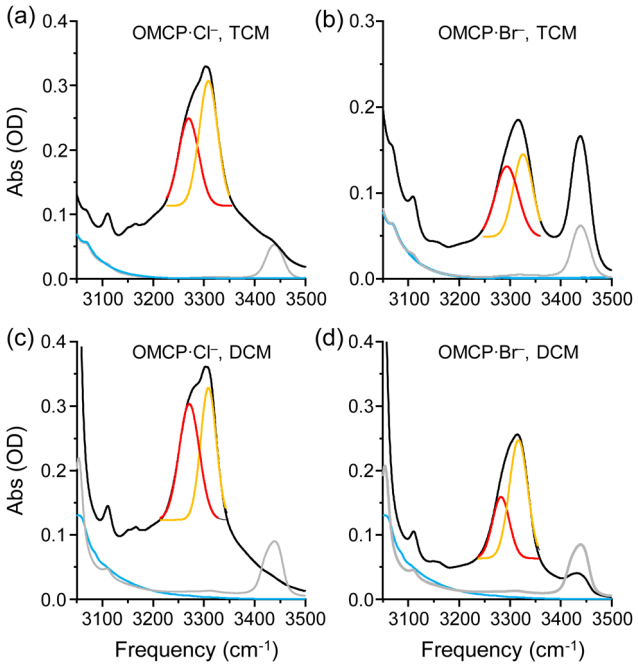

Fig. 3 FTIR spectra of 1 : 5 mixtures of OMCP : X^-. (a) OMCP·Cl^- in TCM. (b) OMCP·Br^- in TCM. (c) OMCP·Cl^- in DCM. (d) OMCP·Br^- in DCM. The spectra of OMCP with no halide salt are shown in gray in each trace. The solvent backgrounds are shown in blue. Gaussian fits to the OMCP·X^- NH stretches are colored red (antisymmetric stretch) and orange (symmetric stretch).

3435 cm^{-1} in both solvents. Upon anion binding, a large red shift of ~100 cm^{-1} is observed in both complexes due to the strong H-bonding interactions between OMCP and each halide. There is also clear asymmetry in the NH absorption feature that arises from an antisymmetric/symmetric NH stretch pair in the cone conformation. The results of fitting the NH stretch features to two Gaussian functions are summarized in Table 1. For OMCP·Cl^- the peak fits are nearly identical between DCM and TCM solutions, consistent with the similar OMCP···Cl^- H-bond distances predicted by the explicit solvent calculations in Fig. 2a. For OMCP·Br^-, on the other hand, both the antisymmetric and symmetric stretches are ~10 cm^{-1} red shifted in DCM compared to TCM. The antisymmetric NH stretch in OMCP·Br^- in DCM is also ~10 cm^{-1} narrower compared to that in TCM. These observations indicate the presence of stronger H-bonding interactions between OMCP and Br^- in DCM, further corroborating the explicit solvent calculations in Fig. 2b. This conclusion is also supported by the much smaller uncomplexed OMCP vibrational signature at 3435 cm^{-1} in DCM compared to TCM in solutions with bromide, suggesting that OMCP·Br^- complex formation is more favorable in DCM. Although more subtle, there is also a smaller uncomplexed OMCP background for the chloride solution in DCM compared to that in TCM. There appears, therefore, to be a surprisingly stronger OMCP···X^- binding interaction in DCM, in contrast to reported halide binding affinities in DCM *vs.* TCM[32,54] and expectations based on the dielectric constants of the two solvents.

Table 1 Frequency and full width at half maximum (FWHM) Gaussian fitting parameters for the antisymmetric and symmetric OMCP·X^- NH stretches shown in Fig. 3. All values are in cm^{-1}

		Antisymmetric stretch		Symmetric stretch	
Solvent	Anion	Frequency	FWHM	Frequency	FWHM
TCM	Cl^-	3270	39	3309	37
	Br^-	3294	45	3325	38
DCM	Cl^-	3271	40	3309	31
	Br^-	3282	33	3316	36

2D IR spectra in the OMCP pyrrole NH stretch region at 150 fs pump–probe waiting time for OMCP·Cl^- and OMCP·Br^- in TCM are presented in Fig. 4a and b, respectively, while those in DCM are given in Fig. 4c and d, respectively. Spectra at later waiting times are provided in Fig. S2 (ESI†). For the OMCP·X^- complexes, strong ground-state bleach features are observed along the diagonal near (ω_1, ω_3) = (3300 cm^{-1}, 3300 cm^{-1}) where the NH stretch intensity maxima appear in the linear absorption spectra for each solution. The excited-state ω_{21} absorption features appear at lower probe frequency near (ω_1, ω_3) = (3350 cm^{-1}, 3100 cm^{-1}) owing to the anharmonicity of the NH stretch potential energy surface. The overlapping antisymmetric/symmetric stretch pair result in broadened, asymmetric 2D lineshapes for both the ground-state bleach and excited-state absorption features. The broadening of the bleaches along ω_1 and the excited-state absorptions along ω_3 are

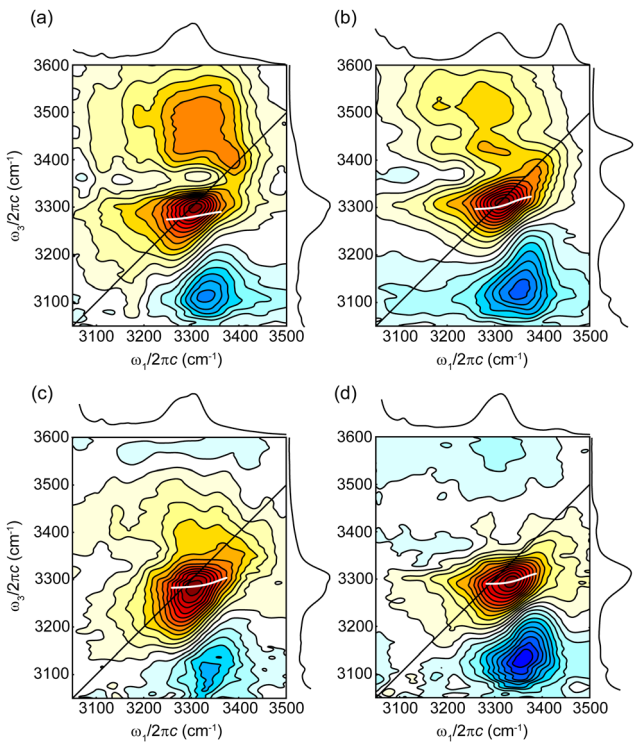

Fig. 4 Isotropic 2D IR spectra at 150 fs pump–probe waiting time in the pyrrole NH stretch region. (a) OMCP·Cl^- in TCM. (b) OMCP·Br^- in TCM. (c) OMCP·Cl^- in DCM. (d) OMCP·Br^- in DCM. The FTIR spectra are shown along the pump and probe axes for comparison. Center line slopes along the NH stretch ground-state bleaches are represented by the superimposed white lines.

indicative of underlying cross peaks between the coupled NH antisymmetric/symmetric stretch pairs. Center line slopes (CLS), a measurement of the degree of inhomogeneous broadening, are also shown superimposed over the NH stretch bleach signals in Fig. 4. The CLS were determined from the first moment of the bleaches in ω_3 along an ω_1 range of $\sim$3275–3375 cm^{-1}. All OMCP complexes display small ($<$0.3) initial CLS values at the earliest pump–probe waiting time, indicating minimal inhomogeneous broadening. This observation is consistent with relatively weak halide–solvent interactions such that small local structural and NH$\cdots$X$^-$ H-bond variations are present within the OMCP·X$^-$ complexes.

A weaker third diagonal bleach feature appears near (ω_1, ω_3) = (3400 cm^{-1}, 3400 cm^{-1}) in each solution with cross peaks to the dominant NH stretch bleach signal. This bleach feature falls well below the NH stretch of uncomplexed OMCP (3435 cm^{-1}) and experiments on OMCP solutions without halide salts yielded insufficient nonlinear signal for the measurement of transient or 2D IR spectra. We would also not expect immediate cross peak signals between complexed and uncomplexed OMCP at the earliest pump–probe waiting time. We, therefore, propose that this higher-energy transition could result from a combination band between the NH stretches and a low-frequency mode that involves side-to-side shuttling motion of the bound anions. Such combination bands were observed by Terry *et al.* in gas-phase OMCP·X$^-$ complexes and were accurately predicted by anharmonic calculations.[40] The position of the combination band $\sim$100 cm^{-1} higher in energy to the NH symmetric stretch in the gas phase is consistent with the location of this additional bleach feature measured in solution. Curiously, there are relatively strong and broad cross peak-like features at (ω_1, ω_3) = (3300 cm^{-1}, $\sim$3500 cm^{-1}) in both TCM solutions. There is weak TCM solvent background that extends into this high-energy spectral region, suggesting potential coupling between the OMCP complexes and TCM solvent molecules. We will discuss this feature in more detail below.

Spectral dynamics

The computational and FTIR spectra presented above point to stronger OMCP·X$^-$ binding interactions in DCM solutions such that the competing anion–solvent interactions are weaker in DCM compared to TCM. To further characterize the interplay between anion–receptor and anion–solvent interactions, we begin by analyzing the isotropic transient absorption spectra. The transient IR spectra of OMCP·Cl$^-$ in TCM is shown in Fig. 5a while that of OMCP·Br$^-$ in DCM is shown in Fig. 5b. Those for the other two solutions (OMCP·Cl$^-$ in DCM and OMCP·Br$^-$ in TCM) are provided in Fig. S3 (ESI†). The decay dynamics of the ω_{21} excited-state NH stretch transitions, which provide a direct measure of the v = 1 vibrational lifetime, are shown in Fig. 5c for all four solutions. Each profile exhibits biexponential decay behavior with an initial fast sub-120 fs component and a slower 1–4 ps component. Although caution must be taken in interpreting the fast component due to pulse overlap effects, the fast decay timescales are consistent with rapid intramolecular relaxation dynamics within the OMCP·X$^-$ complexes due to the strong NH$\cdots$X$^-$ H-bonding interactions.[50,55] The initial NH stretch relaxation components are slightly faster for the two DCM solutions, supportive of stronger OMCP·X$^-$ H-bonding and weaker solvent interactions. In both solvents, the initial decay component is also faster for the chloride complexes compared to bromide, again consistent with stronger H-bonding between OMCP and chloride that leads to faster intramolecular relaxation.

Clear trends are also observed in the slow decay component. OMCP·Cl$^-$ in TCM displays the fastest vibrational relaxation time constant of $\sim$1.7 ps, while that for OMCP·Br$^-$ in TCM is 3.8 ps. Both of these relaxation time constants increase in DCM. The vibrational relaxation of OMCP·Cl$^-$ in DCM slows significantly to 2.9 ps while that of OMCP·Br$^-$ slows more modestly to about 4.0 ps. The large variation in the NH stretch vibrational lifetime dynamics of the chloride complexes demonstrates substantially different solvent interactions between the two solutions. We, therefore, interpret the slow relaxation components to derive largely from intermolecular relaxation of the vibrationally excited OMCP·X$^-$ complexes to the solvent, which occurs more efficiently in TCM compared to DCM.

A stark difference between the two transient absorption spectra shown in Fig. 5 are the long-lived bleach and excited-state signatures observed in OMCP·Cl$^-$ in TCM that are not

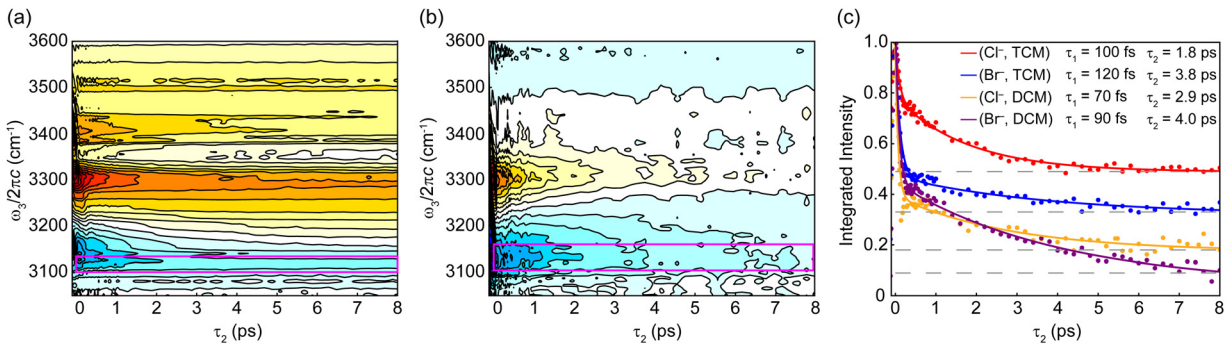

Fig. 5 Isotropic transient absorption spectra of (a) OMCP·Cl$^-$ in TCM and (b) OMCP·Br$^-$ in DCM. (c) Vibrational lifetime decay dynamics measured from the NH stretch excited-state absorption transitions (integration boxes shown in panels (a) and (b)). Red: OMCP·Cl$^-$ in TCM. Blue: OMCP·Br$^-$ in TCM. Orange: OMCP·Cl$^-$ in DCM. Purple: OMCP·Br$^-$ in DCM. Time constants from fits to a biexponential decay function (solid lines) are shown inset in (c). Decay offsets are indicated by the dashed gray lines.

present in OMCP·Br$^-$ in DCM. This can further be seen by the large offset in the excited-state absorption decay profile in Fig. 5c. The excited-state absorption offset is also quite significant in OMCP·Br$^-$ in TCM, while the offsets for the two DCM solutions are smaller but nonzero on an 8 ps timescale. The decay dynamics of the NH stretch ground-state bleach features show similar behavior (Fig. S4, ESI†). The appearance of near-constant background signals at longer waiting times is reminiscent of the so-called "hot ground state" signatures observed in aqueous solutions, a nonequilibrium state where vibrational energy relaxation weakens the water–water and solute–water H-bonds in an equivalent manner to a thermally heated solution at equilibrium.[56,57] The FTIR spectrum of OMCP·Cl$^-$ in TCM at 50 °C is given in Fig. S5 (ESI†). Broadening of the NH stretch absorption profile was observed, with increased absorption at the wings of the transition and decreased intensity at the center of the transition. This change in absorption profile matches the positive–negative–positive profile seen in the late-time transient and 2D IR spectra (note the additional positive feature near ω_3 = 3350 cm^{-1} present in the two TCM solutions). The observed spectral broadening likely derives from larger structural variations and H-bond interaction strengths accessible at higher temperatures. A similar, but weaker, profile is also observed in OMCP·Cl$^-$ in DCM (Fig. S3, ESI†) but is largely absent in OMCP·Br$^-$ in DCM. These observations further corroborate the above interpretations: stronger interactions between TCM and OMCP·X$^-$ complexes lead to more efficient intermolecular vibrational relaxation of excited OMCP·X$^-$ complexes into the solvent resulting in spectroscopic signatures corresponding to a thermally heated sample. That the strength of the hot ground state signatures are anion dependent indicates that the relaxation dynamics are driven by anion–solvent interactions rather than OMCP–solvent interactions.

The dynamics of the weaker 3400 cm^{-1} bleach and 3500 cm^{-1} cross peak features discussed above are provided in Fig. S4 (ESI†). The 3400 cm^{-1} bleaches follow similar dynamic decay profiles as the NH stretch ground-state bleaches, suggesting that this additional feature derives from the OMCP·X$^-$ complexes. Based on the gas-phase spectra reported by Terry *et al.*,[40] we likewise assign this weak feature to a combination band between the NH stretches and a rattling motion of the bound halide. The cross peak that appears near ω_3 = 3500 cm^{-1} in the TCM spectra, on the other hand, are essentially constant over the 8 ps waiting time range measured. The appearance of this feature in only TCM would point to the presence of a solvent-derived background feature since all other species (OMCP, halides, and tetrabutylammonium countercation) are common in the studied solutions. It seems, therefore, that strong and immediate coupling of the NH stretches to first shell TCM molecules are present, consistent with the faster NH stretch vibrational relaxation dynamics and prominent late-time hot ground state signatures in the TCM solutions. Given the relatively high concentrations required for sufficient absorption to measure nonlinear IR spectra, an extended solvation network is not expected (there are about 15 TCM and DCM solvent molecules per OMCP·X$^-$ complex). With only a few solvation shells

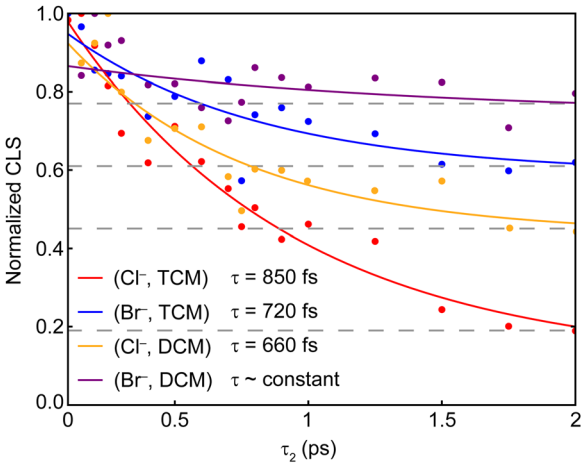

Fig. 6 Center line slope decay dynamics for OMCP·Cl$^-$ in TCM (red), OMCP·Br$^-$ in TCM (blue), OMCP·Cl$^-$ in DCM (orange), and OMCP·Br$^-$ in DCM (purple). Time constants from fits to a monoexponential decay function (solid lines) are shown inset. Decay offsets are indicated by the dashed gray lines.

at best, energy dissipation through the "bulk" solvent will be weak, likely leading to the strong and nearly constant hot ground state spectra observed in TCM. Nevertheless, the presence of this cross peak feature undoubtedly demonstrates that strong coupling exist between OMCP·X$^-$ and first shell TCM molecules.

The decay dynamics of the CLS for each solution are presented in Fig. 6. CLS decay dynamics provide a measure of the frequency–frequency correlation function, that is, the timescale for each oscillator in an inhomogeneous ensemble to explore all possible frequencies arising from structural and/or solvent fluctuations ("spectral diffusion").[42,46,58,59] While the decay dynamics are similar (~700 fs single exponential) between the different solutions, the CLS show modest to minimal decay over the 2 ps measurement range. This observation indicates that the structural distributions are quite static and insensitive to solvent fluctuations due to relatively weak halide–solvent interactions. The exception is OMCP·Cl$^-$ in TCM which displays the greatest degree of spectral diffusion. OMCP·Cl$^-$ in DCM displays the next largest extent of CLS decay. The CLS for OMCP·Br$^-$ in TCM shows an even smaller decay compared to either chloride solution while that of OMCP·Br$^-$ in DCM is essentially constant. The data imply that the strongest halide–solvent interactions occur in OMCP·Cl$^-$ in TCM. Owing to the stronger receptor···Cl$^-$ H-bonding interactions, the OMCP·Cl$^-$ structure and, consequently, the pyrrole NH stretch vibrational frequencies are most sensitive to the competing solvent interactions and fluctuations in the local electric field[60] in the chloride complexes. The structural and NH stretch frequency distributions of the OMCP·Br$^-$ complexes, on the other hand, are less sensitive to the solvent fluctuations.

OMCP-halide binding interactions, solvent effects, and ion pairing

There has been recent discussion over the dominating interactions that contribute to anion–receptor binding. Sengupta *et al.*

decomposed receptor-halide binding energies into electrostatic and nonelectrostatic (induction, dispersion, exchange) contributions for a series of macrocycles.[13] While nonelectrostatic effects were shown to be increasingly important contributors for more complicated macrocycles, electrostatic interactions were found to dominate (~95%) for OMCP·Cl^- and OMCP·Br^-. These calculations, however, were performed on isolated gas-phase complexes and did not take into account solvent effects. In an earlier study, the same authors explored solvent effects on chloride binding with the near-planar macrocycle triazolophane.[15] An inverse relationship between anion binding affinity and the solvent dielectric constant was found, where electrostatic effects dominate for low-dielectric solvents like TCM but become less important as the dielectric constant increases. It was concluded, therefore, that anion binding affinity increases as the competitive binding effects of the solvent decreases. A similar relationship was found by Terry *et al.*, where the dielectric constant for several solvents (TCM, acetone, acetonitrile, dimethyl sulfoxide, water) were compared to the pyrrole NH stretch frequencies from polarizable continuum model (PCM) calculations and solution-phase FTIR measurements.[40] Both the PCM calculations and solution-phase spectra showed an initial rapid blue shift in the NH stretch frequencies with increasing dielectric constant, consistent with a weakening of the halide–OMCP binding interactions with increasingly competitive solvents.

Our measurements, however, show stronger anion–receptor binding interactions and weaker solvent effects in DCM (dielectric constant 8.9) compared to TCM (dielectric constant 4.7), which are inconsistent with the electrostatic/dielectric constant models discussed above. One possible explanation for this apparent discrepancy is the influence of the bulky tetrabutylammonium countercation. Early studies of OMCP·X^- in DCM suggested the possible presence of strong π–cation interactions between alkylammonium cations and the outside ''walls'' of OMCP.[54] In those studies, it was observed that chloride binding affinity decreased with increasing bulkiness of the alkylammonium cation in DCM, while a negligible cation dependence was observed in the similar solvent 1,2-dichloroethane (dielectric constant 10.4). Moreover, the binding affinity of chloride with OMCP in acetonitrile (dielectric constant 37) was reported to be >10-times larger than in DCM.[54] These observations led to the conclusion that alkylammonium cations significantly hinder anion binding with OMCP in DCM, either through direct cation–OMCP interactions and/or cation–anion ion pairing that lowers the amount of free anions in solution. Although the binding affinities of halides with OMCP have not been measured in pure TCM, the binding affinity of chloride in a 1 : 9 v : v mixture of acetonitrile : TCM is even larger than that in pure acetonitrile.[32] This suggests relatively strong anion-OMCP binding is present in TCM solvent, especially when compared to DCM, which is likewise inconsistent with the IR spectra and dynamics reported here.

Indeed, questions regarding the interpretation and method-dependence of anion binding affinity measurements in calix[4]pyrroles have been raised[32,53] and have been shown to not follow any clear trends with respect to common solvent properties.[54] One possible issue with the determination of binding affinities is the usual assumption of a single 1 : 1 receptor : halide equilibrium process. Liu *et al.*, however, demonstrated that several equilibrium processes are at play, including ion pairing.[13] Binding affinities, therefore, appear not to be a robust metric in understanding fundamental anion–receptor interactions in solution. Further, given the low dielectric constant of TCM, one would expect even more perturbative cation effects in TCM compared to DCM. The experimental studies by Liu *et al.* on triazolophane·Cl^- discussed above indicated that ion pairing of the anion–receptor complex with tetrabutylammonium was the dominant binding configuration in TCM, while ion pairing decreased significantly in DCM. It seems more likely, therefore, that cation interactions could be more adversely influencing OMCP-halide binding in TCM compared to in DCM, rather than cation effects being significant in DCM only.

A second explanation for the observed stronger interactions between OMCP·X^- and TCM is the presence of H-bond-like interactions between the CH group of TCM with the halide ions, which is more acidic than the CH groups in DCM.[61] Analyses of crystal structure packing involving halides[62] and species with electronegative groups[63] have identified the persistent presence of H-bond-type interactions with the CH groups of both TCM and DCM solvating molecules. Further, molecular dynamics simulations of chloride in liquid TCM predicted a well-organized, tightly-bound first solvation shell.[64] The suggestion of relatively strong solute-TCM interactions is supported by the explicit solvent calculations presented in Fig. 2, where TCM is predicted to form a closer and near-linear binding interaction with the halides whereas DCM lies further away with a non-ideal H-bonding angle (~150°). Additionally, the observation of strong, long-lived hot ground state signatures in the TCM solutions (Fig. 5 and Fig. S3, ESI†), similar to transient IR spectra of species dissolved in protic solvents like water, infers the presence of H-bond-like solute–solvent interactions between OMCP·X^- complexes and TCM. Based on current definitions and criteria for H-bonding,[65,66] and the presented computational and experimental data, we classify the OMCP·X^-···TCM interaction as a weak H-bond. Further, the near-linear OMCP·X^-···TCM geometry also corresponds to a near-linear alignment of the TCM dipole moment with the halides, resulting in an optimal ion–dipole interaction. On the other hand, the binding geometry of DCM is not only suboptimal for H-bonding but is also non-ideal for an ion–dipole interaction. Instead, the dipoles of the DCM molecules are closer aligned with the overall dipole moment of the OMCP·X^- complexes. H-bonding, ion–dipole, and dipole–dipole interactions, which depend on the molecular-level solute–solvent structures, are not captured by PCM of other implicit electrostatic solvation models.

Overall, the differences in the linear IR spectra between the two solvents are quite subtle (Fig. 3 and Table 1). Transient absorption and 2D IR spectroscopies, however, were able to reveal clear trends between the investigated systems. The

presence of immediate NH stretch to TCM cross peaks and persistent hot ground state spectra indicate efficient intermolecular vibrational energy transfer between OMCP·X$^-$ and TCM *via* a solute–solvent H-bond interaction. The shorter vibrational lifetimes of the OMCP pyrrole NH stretches and greater degree of structural fluctuations in TCM are further supportive of stronger OMCP·X$^-$ interactions with TCM solvent compared to DCM. While we do not see any direct evidence of tetrabutylammonium cation effects, the fact that ion pairing of anion receptors with alkylammonium cations have been demonstrated even at low concentrations in low-dielectric solvents suggests that ion pairing interactions are likely present in the current studies. We conclude, therefore, that the deviation of the observed spectroscopic and dynamical properties of OMCP·X$^-$ in DCM *vs.* TCM from electrostatic solvation models arise from a combination of H-bonding interactions between the halide ions and the solvent CH groups and perturbations due to direct interactions between OCMP with the bulky alkylammonium cations, both of which are stronger in TCM.

IV. Conclusions

The interplay between halide-receptor and halide–solvent interactions in the prototypical calix[4]pyrrole anion receptor OMCP were characterized in TCM and DCM solutions using transient and 2D IR spectroscopies. The IR spectra and dynamics are consistent with greater perturbative effects on halide-receptor binding in TCM solvent compared to in DCM. This was evidenced spectrally by a larger ratio of anion-bound OMCP to uncomplexed OMCP in the linear IR spectra in DCM solvent, a strong off-diagonal cross peak signature between the pyrrole NH stretches and TCM solvent background in the 2D IR spectra, and a prominent late-time constant transient absorption background signal indicative of efficient intermolecular relaxation to TCM. Vibrational dynamics measurements revealed faster pyrrole NH stretch lifetime relaxation and a larger extent of structural fluctuations in TCM. Vibrational dynamics were slower in OMCP·Br$^-$ complexes owing to the weaker H-bonding interactions compared to OMCP·Cl$^-$. The conclusion that TCM more strongly interacts with OMCP·X$^-$ complexes and offers more competitive binding with halides cannot readily be drawn from the linear IR spectra alone, highlighting the importance of vibrational dynamics measurements in the disentanglement of anion–receptor and solvent interactions. While more advanced theoretical modeling is beyond the scope of the present study, our experimental data provide important benchmarks for the development of improved anion–receptor binding models that include explicit solvent and countercation molecules that more accurately and holistically take into account the microscopic structures at play within anion–receptor systems.

Data availability

Cartesian coordinates for all calculated optimized structures are provided in the ESI.† Raw transient and 2D IR data will be made available by the authors upon reasonable request.

Conflicts of interest

There are no conflicts to declare.

Acknowledgements

J. A. F. gratefully acknowledges support from the National Science Foundation through a CAREER Award (Grant CHE-2044927).

References

1 D. H. Evans, Cell signaling and ion transport across the fish gill epithelium, *J. Exp. Zool.*, 2002, **293**, 336–347.
2 V. N. Uversky, C. J. Oldfield and A. K. Dunker, Showing your ID: intrinsic disorder as an ID for recognition, regulation and cell signaling, *J. Mol. Recognit.*, 2005, **18**, 343–384.
3 A. Krężel, Q. Hao and W. Maret, The zinc/thiolate redox biochemistry of metallothionein and the control of zinc ion fluctuations in cell signaling, *Arch. Biochem.*, 2007, **463**, 188–200.
4 I. V. Kolesnichenko and E. V. Anslyn, Practical applications of supramolecular chemistry, *Chem. Soc. Rev.*, 2017, **46**, 2385–2390.
5 P. Bühlmann, E. Pretsch and E. Bakker, Carrier-Based Ion-Selective Electrodes and Bulk Optodes. 2. Ionophores for Potentiometric and Optical Sensors, *Chem. Rev.*, 1998, **98**, 1593–1688.
6 R. Martínez-Máñez and F. Sancenón, Fluorogenic and Chromogenic Chemosensors and Reagents for Anions, *Chem. Rev.*, 2003, **103**, 4419–4476.
7 T. J. Grahame and R. B. Schlesinger, Evaluating the Health Risk from Secondary Sulfates in Eastern North American Regional Ambient Air Particulate Matter, *Inhalation Toxicol.*, 2005, **17**, 15–27.
8 T. R. Crompton, *Determination of Metals in Natural and Treated Water*, CRC Press, London, 2014.
9 M. A. Greer, G. Goodman, R. C. Pleus and S. E. Greer, Health effects assessment for environmental perchlorate contamination: the dose response for inhibition of thyroidal radioiodine uptake in humans, *Environ. Health Perspect.*, 2002, **110**, 927–937.
10 D. K. Nordstrom, Worldwide Occurrences of Arsenic in Ground Water, *Science*, 2002, **296**, 2143–2145.
11 Y. Wang, P. Li, Q. Guo, Z. Jiang and M. Liu, Environmental biogeochemistry of high arsenic geothermal fluids, *Appl. Geochem.*, 2018, **97**, 81–92.
12 A. J. P. Smolders, E. C. H. E. T. Lucassen, R. Bobbink, J. G. M. Roelofs and L. P. M. Lamers, How nitrate leaching from agricultural lands provokes phosphate eutrophication in groundwater fed wetlands: the sulphur bridge, *Biogeochemistry*, 2010, **98**, 1–7.
13 Y. Liu, A. Sengupta, K. Raghavachari and A. H. Flood, Anion Binding in Solution: Beyond the Electrostatic Regime, *Chem.*, 2017, **3**, 411–427.

14 L. M. Eytel, H. A. Fargher, M. M. Haley and D. W. Johnson, The road to aryl CH···anion binding was paved with good intentions: fundamental studies, host design, and historical perspectives in CH hydrogen bonding, *Chem. Commun.*, 2019, **55**, 5195–5206.
15 A. Sengupta, Y. Liu, A. H. Flood and K. Raghavachari, Anion-Binding Macrocycles Operate Beyond the Electrostatic Regime: Interaction Distances Matter, *Chem. – Eur. J.*, 2018, **24**, 14409–14417.
16 P. Molina, F. Zapata and A. Caballero, Anion Recognition Strategies Based on Combined Noncovalent Interactions, *Chem. Rev.*, 2017, **117**, 9907–9972.
17 Y. Hua and A. H. Flood, Click chemistry generates privileged CH hydrogen -bonding triazoles: the latest addition to anion supramolecular chemistry, *Chem. Soc. Rev.*, 2010, **39**, 1262–1271.
18 S. Kubik, Anion Recognition in Aqueous Media by Cyclopeptides and Other Synthetic Receptors, *Acc. Chem. Res.*, 2017, **50**, 2870–2878.
19 P. S. Cremer, A. H. Flood, B. C. Gibb and D. L. Mobley, Collaborative routes to clarifying the murky waters of aqueous supramolecular chemistry, *Nat. Chem.*, 2018, **10**, 8–16.
20 S. Kubik, *Supramolecular Chemistry in Water*, John Wiley & Sons, 2019.
21 L. Escobar and P. Ballester, Molecular Recognition in Water Using Macrocyclic Synthetic Receptors, *Chem. Rev.*, 2021, **121**, 2445–2514.
22 J. Dong and A. P. Davis, Molecular Recognition Mediated by Hydrogen Bonding in Aqueous Media, *Angew. Chem., Int. Ed.*, 2021, **60**, 8035–8048.
23 R. Nishiyabu and P. Anzenbacher, Sensing of antipyretic carboxylates by simple chromogenic calix [4] pyrroles, *J. Am. Chem. Soc.*, 2005, **127**, 8270–8271.
24 R. Nishiyabu, M. A. Palacios, W. Dehaen and P. Anzenbacher, Synthesis, Structure, Anion Binding, and Sensing by Calix[4] pyrrole Isomers, *J. Am. Chem. Soc.*, 2006, **128**, 11496–11504.
25 P. A. Gale, J. L. Sessler, V. Král and V. Lynch, Calix[4]pyrroles: Old Yet New Anion-Binding Agents, *J. Am. Chem. Soc.*, 1996, **118**, 5140–5141.
26 C. J. Woods, S. Camiolo, M. E. Light, S. J. Coles, M. B. Hursthouse, M. A. King, P. A. Gale and J. W. Essex, Fluoride-Selective Binding in a New Deep Cavity Calix[4]pyrrole: Experiment and Theory, *J. Am. Chem. Soc.*, 2002, **124**, 8644–8652.
27 M. P. Wintergerst, T. G. Levitskaia, B. A. Moyer, J. L. Sessler and L. H. Delmau, Calix[4]pyrrole: A New Ion-Pair Receptor As Demonstrated by Liquid–Liquid Extraction, *J. Am. Chem. Soc.*, 2008, **130**, 4129–4139.
28 M. Yano, C. C. Tong, M. E. Light, F. P. Schmidtchen and P. A. Gale, Calix[4]pyrrole-based anion transporters with tuneable transport properties, *Org. Biomol. Chem.*, 2010, **8**, 4356–4363.
29 J. Kříž, J. Dybal, E. Makrlík and Z. Sedláková, Ion *vs.* ion pair receptor: NMR and DFT study of the interaction of Thallium and Cesium ions and ion pairs with *meso*-octamethylcalix[4]pyrrole, *Chem. Phys.*, 2012, **400**, 19–28.
30 E. García-España, M. T. Albelda and J. C. Frías, 2 Inorganic Analytes and Sensors, *Appl. Supramol. Chem.*, 2012, 11.
31 S. Camiolo and P. A. Gale, Fluoride recognition in 'super-extended cavity'calix [4] pyrroles, *Chem. Commun.*, 2000, 1129–1130.
32 F. P. Schmidtchen, Surprises in the Energetics of Host−Guest Anion Binding to Calix[4]pyrrole, *Org. Lett.*, 2002, **4**, 431–434.
33 A. F. Danil De Namor and M. Shehab, Selective Recognition of Halide Anions by Calix[4]pyrrole: A Detailed Thermodynamic Study, *J. Phys. Chem. B*, 2003, **107**, 6462–6468.
34 C. A. Hunter, Quantifying intermolecular interactions: Guidelines for the molecular recognition toolbox, *Angew. Chem., Int. Ed.*, 2004, **43**, 5310–5324.
35 V. P. Solov'ev, N. N. Strakhova, O. A. Raevsky, V. Rüdiger and H.-J. Schneider, Solvent effects on crown ether complexations, *J. Org. Chem.*, 1996, **61**, 5221–5226.
36 M. V. Rekharsky, T. Mori, C. Yang, Y. H. Ko, N. Selvapalam, H. Kim, D. Sobransingh, A. E. Kaifer, S. Liu, L. Isaacs, W. Chen, S. Moghaddam, M. K. Gilson, K. Kim and Y. Inoue, A synthetic host–guest system achieves avidin-biotin affinity by overcoming enthalpy–entropy compensation, *Proc. Natl. Acad. Sci. U. S. A.*, 2007, **104**, 20737–20742.
37 C. L. D. Gibb and B. C. Gibb, Anion Binding to Hydrophobic Concavity Is Central to the Salting-in Effects of Hofmeister Chaotropes, *J. Am. Chem. Soc.*, 2011, **133**, 7344–7347.
38 K. I. Assaf, M. S. Ural, F. Pan, T. Georgiev, S. Simova, K. Rissanen, D. Gabel and W. M. Nau, Water Structure Recovery in Chaotropic Anion Recognition: High-Affinity Binding of Dodecaborate Clusters to γ-Cyclodextrin, *Angew. Chem., Int. Ed.*, 2015, **54**, 6852–6856.
39 S. J. Pike, J. J. Hutchinson and C. A. Hunter, H-Bond Acceptor Parameters for Anions, *J. Am. Chem. Soc.*, 2017, **139**, 6700–6706.
40 L. M. Terry, M. M. Foreman, A. P. Rasmussen, A. B. McCoy and J. M. Weber, Probing Ion–Receptor Interactions in Halide Complexes of Octamethyl Calix[4]Pyrrole, *J. Am. Chem. Soc.*, 2024, **146**, 12401–12409.
41 W. Cao and X.-B. Wang, Organic Molecules Mimic Alkali Metals Enabling Spontaneous Harpoon Reactions with Halogens, *Chem. – Eur. J.*, 2024, **30**, e202400038.
42 P. Hamm and M. T. Zanni, *Concepts and Methods of 2D Infrared Spectroscopy*, Cambridge UP, Cambridge, 2011.
43 M. F. Kropman and H. J. Bakker, Femtosecond mid-infrared spectroscopy of aqueous solvation shells, *J. Chem. Phys.*, 2001, **115**, 8942–8948.
44 S. Park, D. E. Moilanen and M. D. Fayer, Water Dynamics The Effects of Ions and Nanoconfinement, *J. Phys. Chem. B*, 2008, **112**, 5279–5290.
45 M. D. Fayer, Dynamics of Water Interacting with Interfaces, Molecules, and Ions, *Acc. Chem. Res.*, 2012, **45**, 3–14.
46 D. E. Moilanen, N. E. Levinger, D. B. Spry and M. D. Fayer, Confinement or the Nature of the Interface? Dynamics of Nanoscopic Water, *J. Am. Chem. Soc.*, 2007, **129**, 14311–14318.
47 M. D. Fayer and N. E. Levinger, Analysis of Water in Confined Geometries and at Interfaces, *Annu. Rev. Anal. Chem.*, 2010, **3**, 89–107.

48 E. A. Perets, P. E. Videla, E. C. Y. Yan and V. S. Batista, Chiral Inversion of Amino Acids in Antiparallel β-Sheets at Interfaces Probed by Vibrational Sum Frequency Generation Spectroscopy, *J. Phys. Chem. B*, 2019, **123**, 5769–5781.

49 M. L. McDermott, H. Vanselous, S. A. Corcelli and P. B. Petersen, DNA's Chiral Spine of Hydration, *ACS Cent. Sci.*, 2017, **3**, 708–714.

50 J. L. S. Dean, V. S. Winkler, M. A. Boyer, E. L. Sibert and J. A. Fournier, Investigating Intramolecular H Atom Transfer Dynamics in β-Diketones with Ultrafast Infrared Spectroscopies and Theoretical Modeling, *J. Phys. Chem. A*, 2023, **127**, 9258–9272.

51 M. J. Frisch, G. W. Trucks, H. B. Schlegel, G. E. Scuseria, M. A. Robb, J. R. Cheeseman, G. Scalmani, V. Barone, B. Mennucci, G. A. Petersson, H. Nakatsuji, M. Caricato, X. Li, H. P. Hratchian, A. F. Izmaylov, J. Bloino, G. Zheng, J. L. Sonnenberg, M. Hada, M. Ehara, K. Toyota, R. Fukuda, J. Hasegawa, M. Ishida, T. Nakajima, Y. Honda, O. Kitao, H. Nakai, T. Vreven, J. A. Montgomery Jr, J. E. Peralta, F. Ogliaro, M. J. Bearpark, J. Heyd, E. N. Brothers, K. N. Kudin, V. N. Staroverov, R. Kobayashi, J. Normand, K. Raghavachari, A. P. Rendell, J. C. Burant, S. S. Iyengar, J. Tomasi, M. Cossi, N. Rega, N. J. Millam, M. Klene, J. E. Knox, J. B. Cross, V. Bakken, C. Adamo, J. Jaramillo, R. Gomperts, R. E. Stratmann, O. Yazyev, A. J. Austin, R. Cammi, C. Pomelli, J. W. Ochterski, R. L. Martin, K. Morokuma, V. G. Zakrzewski, G. A. Voth, P. Salvador, J. J. Dannenberg, S. Dapprich, A. D. Daniels, Ö. Farkas, J. B. Foresman, J. V. Ortiz, J. Cioslowski and D. J. Fox, *Gaussian 09*, Gaussian, Inc., Wallingford, CT, USA, 2009.

52 W. P. Van Hoorn and W. L. Jorgensen, Selective Anion Complexation by a Calix[4]pyrrole Investigated by Monte Carlo Simulations, *J. Org. Chem.*, 1999, **64**, 7439–7444.

53 J. R. Blas, M. Márquez, J. L. Sessler, F. J. Luque and M. Orozco, Theoretical Study of Anion Binding to Calix[4]pyrrole: the Effects of Solvent, Fluorine Substitution, Cosolute, and Water Traces, *J. Am. Chem. Soc.*, 2002, **124**, 12796–12805.

54 J. L. Sessler, D. E. Gross, W.-S. Cho, V. M. Lynch, F. P. Schmidtchen, G. W. Bates, M. E. Light and P. A. Gale, Calix[4]pyrrole as a Chloride Anion Receptor: Solvent and Countercation Effects, *J. Am. Chem. Soc.*, 2006, **128**, 12281–12288.

55 K. Ramasesha, L. De Marco, A. Mandal and A. Tokmakoff, Water vibrations have strongly mixed intra- and intermolecular character, *Nat. Chem.*, 2013, **5**, 935–940.

56 L. De Marco, J. A. Fournier, M. Thamer, W. Carpenter and A. Tokmakoff, Anharmonic exciton dynamics and energy dissipation in liquid water from two-dimensional infrared spectroscopy, *J. Chem. Phys.*, 2016, **145**, 094501.

57 A. J. Lock, S. Woutersen and H. J. Bakker, Ultrafast energy equilibration in hydrogen-bonded liquids, *J. Phys. Chem. A*, 2001, **105**, 1238–1243.

58 J. B. Asbury, T. Steinel, C. Stromberg, S. A. Corcelli, C. P. Lawrence, J. L. Skinner and M. D. Fayer, Water Dynamics: Vibrational Echo Correlation Spectroscopy and Comparison to Molecular Dynamics Simulations, *J. Phys. Chem. A*, 2004, **108**, 1107–1119.

59 S. Park, D. E. Moilanen and M. D. Fayer, Water DynamicsThe Effects of Ions and Nanoconfinement, *J. Phys. Chem. B*, 2008, **112**, 5279–5290.

60 J. D. Smith, R. J. Saykally and P. L. Geissler, The Effects of Dissolved Halide Anions on Hydrogen Bonding in Liquid Water, *J. Am. Chem. Soc.*, 2007, **129**, 13847–13856.

61 H. E. Gottlieb, V. Kotlyar and A. Nudelman, NMR Chemical Shifts of Common Laboratory Solvents as Trace Impurities, *J. Org. Chem.*, 1997, **62**, 7512–7515.

62 P. V. Gushchin, G. L. Starova, M. Haukka, M. L. Kuznetsov, I. L. Eremenko and V. Yu, Kukushkin, Chloride−Chloroform Clusters Exhibiting Weak Hydrogen and Halogen Bondings Are Fully Characterized in the Solid State by X-ray Diffraction, *Cryst. Growth Des.*, 2010, **10**, 4839–4846.

63 F. H. Allen, P. A. Wood and P. T. Galek, Role of chloroform and dichloromethane solvent molecules in crystal packing: an interaction propensity study, *Acta Crystallogr., Sect. B: Struct. Sci., Cryst. Eng. Mater.*, 2013, **69**, 379–388.

64 T.-M. Chang and L. X. Dang, Ion Solvation in Polarizable Chloroform: A Molecular Dynamics Study, *J. Phys. Chem. B*, 1997, **101**, 10518–10526.

65 E. Arunan, G. R. Desiraju, R. A. Klein, J. Sadlej, S. Scheiner, I. Alkorta, D. C. Clary, R. H. Crabtree, J. J. Dannenberg, P. Hobza, H. G. Kjaergaard, A. C. Legon, B. Mennucci and D. J. Nesbitt, Definition of the hydrogen bond (IUPAC Recommendations 2011), *Pure Appl. Chem.*, 2011, **83**, 1637–1641.

66 G. R. Desiraju, A Bond by Any Other Name, *Angew. Chem., Int. Ed.*, 2011, **50**, 52–59.

